CFD modeling using PDF approach for investigating the flame length in rotary kilns

H. F. Elattar, E. Specht, A. Fouda & Abdullah S. Bin-Mahfouz

Heat and Mass Transfer
Wärme- und Stoffübertragung

ISSN 0947-7411
Volume 52
Number 12

Heat Mass Transfer (2016) 52:2635-2648
DOI 10.1007/s00231-016-1768-7

Springer

Heat Mass Transfer (2016) 52:2635–2648
DOI 10.1007/s00231-016-1768-7

ORIGINAL

CFD modeling using PDF approach for investigating the flame length in rotary kilns

H. F. Elattar[1,2] · E. Specht[3] · A. Fouda[1,4] · Abdullah S. Bin-Mahfouz[5]

Received: 7 April 2015 / Accepted: 28 January 2016 / Published online: 12 February 2016

Abstract Numerical simulations using computational fluid dynamics (CFD) are performed to investigate the flame length characteristics in rotary kilns using probability density function (PDF) approach. A commercial CFD package (ANSYS-Fluent) is employed for this objective. A 2-D axisymmetric model is applied to study the effect of both operating and geometric parameters of rotary kiln on the characteristics of the flame length. Three types of gaseous fuel are used in the present work; methane (CH_4), carbon monoxide (CO) and biogas (50 % CH_4 + 50 % CO_2). Preliminary comparison study of 2-D modeling outputs of free jet flames with available experimental data is carried out to choose and validate the proper turbulence model for the present numerical simulations. The results showed that the excess air number, diameter of kiln air entrance, radiation modeling consideration and fuel type have remarkable effects on the flame length characteristics. Numerical correlations for the rotary kiln flame length are presented in terms of the studied kiln operating and geometric parameters within acceptable error.

✉ H. F. Elattar
hassan.alattar@bhit.bu.edu.eg

[1] Mechanical Engineering Department, Faculty of Engineering, University of Jeddah, 21589 Jeddah, Kingdom of Saudi Arabia

[2] Mechanical Engineering Department, Faculty of Engineering, Benha University, Benha 13511, Qalyubia, Egypt

[3] Institute of Fluid Dynamics and Thermodynamics, Otto-von-Guericke-University of Magdeburg, Universitätsplatz 2, 39106 Magdeburg, Germany

[4] Mechanical Power Engineering Department, Faculty of Engineering, Mansoura University, 35516 El-Mansoura, Egypt

[5] Chemical Engineering Department, Faculty of Engineering, University of Jeddah, 21589 Jeddah, Kingdom of Saudi Arabia

List of symbols

$A_{a,i}$	Air entrance area (m^2)
C_2, $C_{I\varepsilon}$	Turbulence model constants
D	Diameter of kiln (m)
$d_{a,i}$	Air entrance diameter (m)
d_o	Fuel nozzle diameter (m)
d_p	Primary air nozzle diameter (m)
f	Mixture fraction, $f = \phi/(\phi + L)$
f_a	Axial mean mixture fraction
F_i	External body force (N)
f_o	Fuel mean mixture fraction
f_{st}	Stoichiometric mean mixture fraction, $f_{st} = 1/(1 + L)$
G	Incident radiation (W/m^2)
g_i	Gravitational acceleration (m/s^2)
I	Turbulence intensity
k	Turbulent kinetic energy (m^2/s^2)
L	Stoichiometric air to fuel mass ratio (kg_{air}/kg_{fuel})
L_f	Overall confined jet flame length (m)
p	Pressure (Pa)
q_r	Radiation heat flux (w/m^2)
R	Radius of kiln (m)
$r_{a,i}$	Radius of air entrance (m)
Re_{DH}	Reynolds number based on hydraulic diameter
T	Local temperature (K)
T_a	Axial temperature (K)
T_{air}	Air temperature (K)
T_o	Fuel temperature (K)
u	Mean axial velocity (m/s)
u_a	Axial velocity of the mixture/flame (m/s)
u_i, u_j	Velocity components in x and y directions

	(m/s)
u_o	Fuel velocity at the nozzle (m/s)
u_p	Primary air velocity at the nozzle (m/s)
v	Mean radial velocity (m/s)
w	Mean tangential velocity (m/s)
x	Axial distance from burner (m)
Z_i	Mass fraction of species i
ε	Turbulent dissipation rate (m^2/s^3)
κ	Absorption coefficient (1/m)
λ	Excess air number
μ	Dynamic viscosity (Pa.s)
μ_t	Turbulent viscosity (kg/m.s)
ν	Kinematic viscosity (m^2/s)
ρ	Density (kg/m^3)
ρ_o	Density of fuel (kg/m^3)
ρ_{st}	Stoichiometric density (density of combustion gas at stoichiometric mixture fraction) (kg/m^3)
σ	Stefan-Boltzmann constant (5.669×10^{-8} W/m^2K^4)
σ_ε	Turbulent Prandtl number for the turbulence kinetic energy dissipation rate
σ_k	Turbulent Prandtl number for the turbulence kinetic energy
σ_t	Turbulent Prandtl number, $\sigma_t = \mu_t c_p/k_t = 0.85$
$\tau_{i,j}$	Stress tensor (Pa)
ϕ	Equivalence ratio, $\phi = (air/fuel)_{stoichiometric}/(air/fuel)_{actual}$
2-D	Two dimensional
3-D	Three dimensional
CFD	Computational fluid dynamics
CPU	Central processing unit
DLR	Deutschland fur Lüft und Raumfahrt (German Aerospace Center)
PDF	Probability density function
RANS	Reynolds averaged Navier–Stokes
RSM	Reynolds stress model
SWF	Standard wall functions
WSGGM	Weighted sum of gray gases model

1 Introduction

The devices that performs calcination processes which are also known as pyroprocessing devices have a key function of elevating the materials to a high temperature (calcination) in a continuous process are also known as rotary kilns [1]. Many industrial applications including cement industries, metallurgy and burning of waste things are performed by rotary kilns [2]. Rotary kilns can work under high heating temperature; burning the lime to 1200 °C [3], firing the cement clinker to 2000 °C, calcinations of petroleum coke (1100 °C) [4] and processing calcinations for aluminum oxide, reaching a high temperature of 1300 °C. All are designed to process under high temperature [5, 6]. The main industrial applications of rotary kilns are cement industries [7]. Moreover, rotary kilns are used in the incineration of waste materials due to having the features of handling various supply materials with different heating value and have the abilities to burn the solid wastes at the exit site effectively [8]. Enhancing the heterogeneous combustion can be done by hazardous waste incinerators that work mostly at deep beds and possess a second combustion chamber rotary kiln [9]. In addition, the gasification process of waste tires that produces an activated carbon material [10, 11] and the clearing up of the contaminated soil are also common applications of the rotary kilns in the industrial field [12, 13]. The three main purposes of rotary kilns are used: reacting, helping in dryness of solid material, and heating material. In many cases, rotary kilns are used to accomplish all of these processes.

Analyzing and solving problems related to the rotary kilns design and their operating parameters in the last few decades has been performed using CFD approach that has been demonstrated to be a powerful and versatile tool for these tasks. In the design process, heat removal from flame, solids flow along the kiln, solid–gas reaction and mass transfer are crucial aspects in designing a new rotary kiln [14]. The performance of rotary kiln is affected by the rate of heat transfer from flame to solids. The rate of heat transfer, product quality, refractory life and emissions are strongly influenced by the flame behavior (i.e. length, shape and intensity). For instance, flame pattern has considerably influence on the mid kiln rings formation that have disagreeing impact on the kiln performance and might cause more maintenance work and repairs. A large variation in gas temperatures can be a result of unstable flame. In addition, the refractory lining can be damaged by short bushy flame, weak flame may not deliver enough heat for reaction process. Moreover, the flame properties such as shape and length can be influenced by operating parameters such as the kind of fuel used and fuel flow rate [15]. The investigation of flame length is a challenging mission due to the rotary kiln operating parameters fluctuations [16].

By reviewing the previous works, it turned out that there is somehow lack in studying the flame length characteristics as a kiln heat source and the flow pattern inside the rotary kilns. Moreover, there are still many operating parameters and designing aspects of rotary kilns that are under investigations such as the effects of excess air number, the air entrance diameter, the fuel type and the radiation modeling on the length of flame. This study tries to find a new effective parameters on rotary kiln flame length. The analysis of a rotary kiln jet flame that functions under three different types of gaseous fuels is performed by a 2-D computational simulation using PDF approach. The objectives of this study are to simulate the rotary kiln and to

examine the influence of kiln geometry with different operating parameters on flame length.

The simulation results are presented in the form of axial centerline mean mixture fraction profiles. In addition, the velocity vectors and temperature contours are presented to display the flame pattern in the kiln. These parameters are investigated carefully to control the flame length, which has essential effect on thermal processes and product quality inside the kiln. Finally, valuable design guidelines and numerical flame length correlations are presented and discussed.

2 Physical model, boundary conditions and mesh generation

For investigating the effect of different kiln geometric and its operating parameters on the flame length, Fig. 1 shows a schematic graph of confined non-premixed flame configuration that was presented by Elattar et al. [17]. A simple burner with changeable air entrance area ($A_{a,i}$) can be adjusted by adjusting air entrance diameter ($d_{a,i}$) as presented in Fig. 1. The burner has a thermal power that varies from 0.69 to 1.97 MW based on fuel kind and it is 50 mm in diameter. The fuel enters the kiln with a uniform axial velocity of 30 m/s and with a temperature of 20 °C. The excess air number (λ) changes from 1 to 2.5 (e.g. λ = 1.1 implies that 10 % more than the needed stoichiometric air is being utilized). Three kinds of gaseous fuels were used in this study; CH_4, CO and *biogas* which have broad range of stoichiometric air demand (mass basis). A preliminary comparison study between 2-D and 3-D simulations was performed and the results reviled that the maximum error obtained for axial velocity (u_a), axial temperature and axial mean mixture fraction (f_a) were 5, 2, and 6 %, respectively. Therefore, 2-D axisymmetric simulation is sufficient to carry out the present study within acceptable error for time and cost savings.

A two dimensional (2-D) computational domain is available in Fig. 2a and computational mesh of the rotary kiln is available in Fig. 2b as presented by Elattar et al. [17]. The

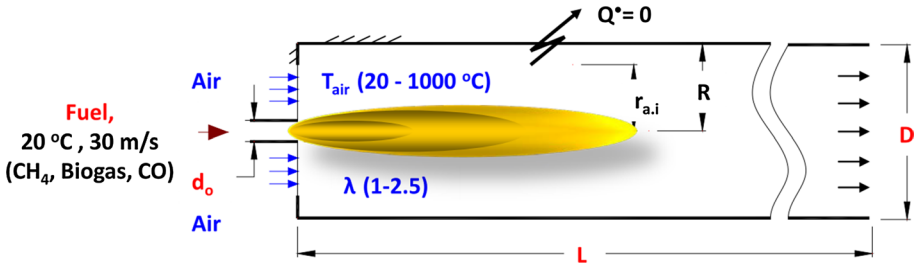

Fig. 1 Physical model schematic of rotary kiln [17]

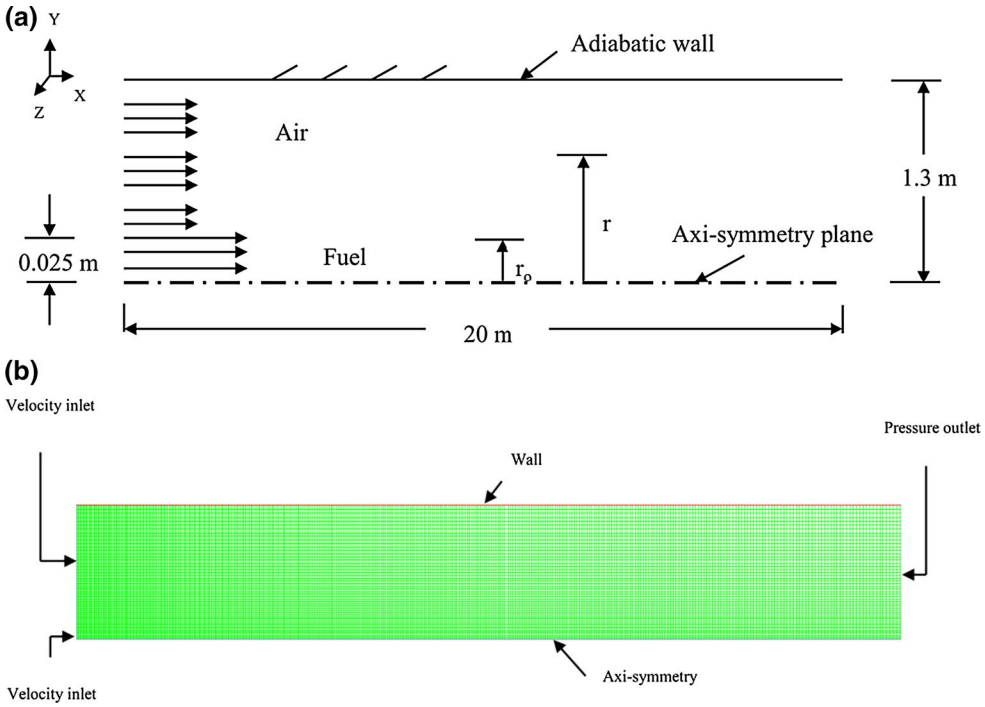

Fig. 2 2D rotary kiln model [17]: **a** computational domain, **b** mesh with boundary types

Table 1 Dimensionless flame length for different number of cells

No. of cells	Dimensionless flame length (L_f/d_o)
3×10^3	196.5
5×10^3	194.2
7.2×10^3	192.9
11×10^3	192.9
15×10^3	190.9
20×10^3	190.0
25×10^3	189.9
30×10^3	186.2
35×10^3	186.0
39.9×10^3	185.9
59.5×10^3	186.0
79.8×10^3	186.6
100×10^3	186.1

boundary conditions of the studied domain are: velocity inlet for the oxidizer (air) and fuel and pressure outlet for combustion gases at the kiln exit. Adiabatic walls for the kiln surfaces. The velocity and temperature are identified uniform at the inlet boundaries. To investigate the influence of confinements on the flame length, the following consideration is taken into account; the physical model is built to have a shape of axisymmetric kiln with 20 m in length and 2.6 m in diameter. In order to reduce the computational cost, only hemi-kiln is considered for the current study as illustrated in Fig. 2a. The preprocessing tool in ANSYS package with 30×10^3 structured and quadrilateral cells are used to generate the mesh. At the flame region, a fine grid near the burner is made by the conventional wall-function. The computational mesh with boundary conditions of the 2-D domain of rotary kiln model is shown in Fig. 2b.

In order to ensure that the obtained result is independent of the mesh resolution, a grid independence study is performed. Therefore, numbers of 2-D grids with different resolutions are generated to this purpose. Different numbers of cells varying from 3×10^3 to 100×10^3 cells that are examined on flame length convergence are tabulated in Table 1. The output of the grid independence study shows that the grid with cells $>30 \times 10^3$ cells have a slight variation (less than 0.2 % of flame length). Therefore, computational grid with 30×10^3 cells is selected to perform this study.

3 Methodology

3.1 Turbulence model selection and validation

In order to choose the proper turbulent model in the current study, different numerical simulations were applied using different turbulent models and then these results

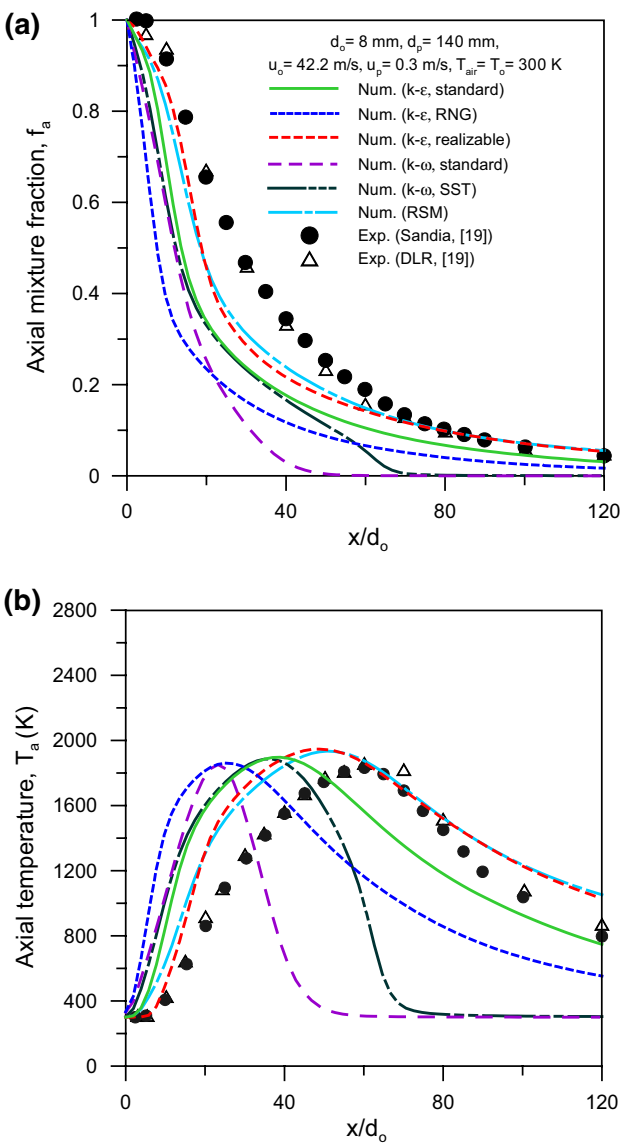

Fig. 3 Comparisons of different turbulence models with experimental results [18]: **a** axial mixture fraction, **b** axial temperature

were compared to available experimental data as presented by Elattar et al. [18]. The axial centerline mixture fraction and temperature results comparison between present simulation and available published experimental data [19] are presented in Fig. 3a, b, respectively. As shown in the figures, the realizable k-ε turbulent model provides the closest model to the published experimental data in comparison to other turbulent models applied. Moreover, the realizable k-ε model turbulent model is considered very similar in behavior to the Reynolds-Stress-Model (RSM) which requires more computational time to apply [20] if it compared to other turbulent models as seen in Table 2. In conclusion, the realizable k-ε turbulence model provides adequate

Table 2 CPU computational time for different turbulence models

Turbulence model	RNG k-ε	Realizable k-ε	k-ω	RSM
CPU time	10–15 % > standard k-ε CPU time	Slightly > standard k-ε CPU time	≅ standard k-ε CPU time	50–60 % > standard k-ε CPU time and 15–20 % more memory

agreement with the compared experimental results, hence it is recommended to implement the present simulation.

3.2 Mathematical formulas approach and assumptions

In order to resolve the energy equation and radiation model, Reynolds averaged Navier–Stokes (RANS) equations and species transport, a need for CFD flow formula that depends on finite volume method (ANSYS-Fluent) is deemed essential for this study to be applied. The following assumptions are taken into consideration; axisymmetric model is applied and the flow is considered as steady and incompressible. There was not any considerable influence on the flame performance and its aerodynamics made by percentage of bed fill, rotation speed, and buoyancy [21]. The adiabatic walls are assumed and the wall construction is not considered in this study (i.e. wall heat transfer = 0, wall inner side emissivity = 1 and thickness of wall = 0). Therefore, these assumptions proceed to relatively approximated and acceptable results.

Equation (1) is the continuity equation of steady gas phase flow, where the source term, S_m is a product from fuel injection. The momentum equation that is given in Eq. (2) is composed of velocity in a 3-D coordinate system. The pressure, turbulent shear stresses, gravitational force (buoyancy effects), and the source terms are presented in Eq. (2).

$$\frac{\partial}{\partial x_i}(\rho u_i) = S_m \tag{1}$$

$$\frac{\partial}{\partial x_j}\left(\rho u_i u_j\right) = -\frac{\partial p}{\partial x_i} + \frac{\partial \tau_{ij}}{\partial c_j} + \rho g_i + F_i + S_m. \tag{2}$$

The current research study applies various turbulence models in order to achieve the appropriate model that generates accurate results with agreement to the existing experimental results. As illustrated in Fig. 3, the realizable k-ε turbulence model is found to be in accordance with the published experimental results from previous studies. The instantaneous Navier–Stokes formula is the generator of the realizable k-ε turbulence model, where the word "realizable" implies that the model is based on particular mathematical restrains on the Reynolds stresses and compatible with the physics of turbulent flows [22].

The analytical deduction of the realizable k-ε turbulence model is different from the standard k-ε and the RNG k-ε models in terms of its constants, terms and functions in the transport formulas for k and ε. The transport formulas for the realizable k-ε model are provided in Eqs. (3) and (4).

$$\frac{\partial}{\partial x_j}(\rho k u_j) = \frac{\partial}{\partial x_j}\left[\left(\mu + \frac{\mu_t}{\sigma_k}\right)\frac{\partial k}{\partial x_j}\right] + G_k + G_b - \rho\varepsilon \tag{3}$$

$$\begin{aligned}\frac{\partial}{\partial x_j}(\rho \varepsilon u_j) = {} & \frac{\partial}{\partial x_j}\left[\left(\mu + \frac{\mu_t}{\sigma_\varepsilon}\right)\frac{\partial \varepsilon}{\partial x_j}\right] \\ & + \rho C_1 S\varepsilon - \rho C_2 \frac{\varepsilon^2}{k + \sqrt{\nu\varepsilon}} + C_{1\varepsilon}\frac{\varepsilon}{k} C_{3\varepsilon} G_b\end{aligned} \tag{4}$$

where, G_k symbolizes the generation of turbulence kinetic energy due to the mean velocity gradients and G_b due to the buoyancy as presented in Eqs. (3) and (4), σ_k and σ_ε are the turbulent Prandtl numbers for k and ε, C_2 and $C_{1\varepsilon}$ are constant values.The turbulent intensity (I) can be estimated based on the following equation [20]:

$$I = 0.16(\mathrm{Re}_{DH})^{-0.125}. \tag{5}$$

In the current simulation, the turbulent intensities are taken as 10 and 5 % for air and fuel inlets, respectively. These values are the average values according to the air and fuel Reynolds numbers that vary with air and fuel sides studied variables (i.e. $\lambda(d_{a,i}/d_o)$ and fuel type).

The chemical reaction simulation is the basis for non-premixed combustion and PDF models. The non-premixed combustion modeling technique proposes several advantages over the finite rate formulation, where the model is able to predict radical species, dissociation effects, and accurate turbulence-chemistry coupling. This approach is considered computationally efficient since it requires fewer formulas to resolve. The non-premixed combustion modeling can be applied only when the system of reacting flow has the following criteria: the flow is in turbulent state, the reaction includes fuel stream and an oxidant stream. Moreover, the chemical reaction kinetics state has to be quick so that the flow can achieve near chemical equilibrium state [20].

The PDF is a preferred approach when the combustion manner including turbulent flow due to the fluctuation of turbulent mixing properties. In this study, β-PDF model is

applied for better outputs for turbulent non-premixed combustion flow over other PDF models [23]. β-PDF model is specified by two parameters; mean scalar quantity and its variance. In order to avoid complexity in resolving the species transport formula, the mixture fraction (f) in the presumed β-PDF depends on species i mass fraction (Z_i) and calculated as follows:

$$f = \frac{Z_i - Z_{i,ox}}{Z_{i,fuel} - Z_{i,ox}}. \tag{6}$$

The subscript "*ox*" represents the oxidizer inlet value and subscript "*fuel*" represents the fuel stream inlets. The f equals one for the fuel flow, and zero for the oxidizer flow and its value varies from zero to one ($f = 0-1$) throughout the flow field.

The transport formulas of mean mixture fraction, $\bar{f}$ and its variance, $\overline{f'^2}$ are presented in Eqs. (7) and (8).

$$\frac{\partial}{\partial t}(\rho\bar{f}) + \frac{\partial}{\partial x_j}(\rho u_j \bar{f}) = \frac{\partial}{\partial x_j}\left(\frac{\mu_t}{\sigma_t}\frac{\partial \bar{f}}{\partial x_j}\right) \tag{7}$$

$$\frac{\partial}{\partial t}(\rho\overline{f'^2}) + \frac{\partial}{\partial x_j}(\rho u_j \overline{f'^2}) = \frac{\partial}{\partial x_j}\left(\frac{\mu_t}{\sigma_t}\frac{\partial \overline{f'^2}}{\partial x_j}\right) + C_g\mu_t\left(\frac{\partial \bar{f}}{\partial x_j}\right)^2 - C_d\rho\frac{\varepsilon}{k}\overline{f'^2} \tag{8}$$

where, $f' = f - \bar{f}$, the following default values for the constants are: $\sigma_{t=}$ 0.85, $C_{g=}$ 2.86, and $C_d = 2.0$. The chemical reaction is summarized to one parameter, f as a power feature of the mixture fraction modeling approach. All thermochemical scalars (species fractions, density, and temperature) are exclusively related to the mixture fraction at chemical equilibrium state. The instant values of mass fractions, density and temperature rely directly on the instant mixture fraction, f and given as:

$$\phi_i = \phi_i(f) \tag{9}$$

$$\phi_i = \phi_i(f, H). \tag{10}$$

In Eqs. (9) and (10), ϕ_i symbolizes the instant species mass fraction, density, or temperature for adiabatic and non-adiabatic systems, respectively and H is the instantaneous enthalpy. The mean values of fluctuating scalars which are computed from Eqs. (7) and (8) can lead to the identification of the turbulent reacting flow model; these values depend on the turbulence-chemistry interaction model. PDF model is the best fit if the non-premixed combustion model is applied. It is written as $p(f)$ and represented the portion of time that the fluid stays in the vicinity of the state f. The mean values of species concentration and temperature can be obtained by this approach. The average mass fraction of species and temperature, $\bar{\phi}_i$ can be obtained as follows:

$$\bar{\phi}_i = \int_0^1 p(f)\,\phi_i(f)\,df \tag{11}$$

$$\bar{\phi}_i = \int_0^1 p(f)\,\phi_i(f, \bar{H})\,df. \tag{12}$$

Equations (11) and (12) denote the average mass fraction of species and temperature for adiabatic and non-adiabatic systems.

Correspondingly, the mean time-averaged fluid density, $\bar{\rho}$, can be calculated as

$$\frac{1}{\bar{\rho}} = \int_0^1 \frac{p(f)}{\rho(f)}df \tag{13}$$

where, $p(f) = \frac{f^{\alpha-1}(1-f)^{\beta-1}}{\int f^{\alpha-1}(1-f)^{\beta-1}df}$; α and β are $\alpha = \bar{f}\left[\frac{\bar{f}(1-\bar{f})}{\overline{f'^2}} - 1\right], \beta = (1-\bar{f})\left[\frac{\bar{f}(1-\bar{f})}{\overline{f'^2}} - 1\right]$.

In order to solve the transport equation of mean enthalpy, $\bar{H}$ and to predict $\bar{\phi}_i$ for non-adiabatic system, Eq. (14) is applied:

$$\frac{\partial}{\partial t}(\rho\bar{H}) + \nabla\cdot(\rho\vec{v}\bar{H}) = \nabla\cdot\left(\frac{k_t}{c_p}\nabla\bar{H}\right). \tag{14}$$

The species thermal properties are functions of temperature and standard atmospheric pressure (1.013×10^5 Pa). In order to solve the enthalpy, energy Eq. (15) is applied.

$$\frac{\partial}{\partial x_i}(\rho v_i h) = \frac{\partial}{\partial x_i}\left(\Gamma_h\frac{\partial h}{\partial x_i}\right) + S_h. \tag{15}$$

The source term S_h in Eq. (15) comprises the heat transfer rate for combustion and radiation.

For determining the radiation flux inside the rotary kiln, the P-1 radiation model is applied. This P-1 radiation model is considered simple in comparison to the more general P-N radiation models [24, 25]. Moreover, P-1 model has a feature of requiring only a little computer processor working units of the Central Processing Unit (CPU) where it can be considered in various complicated geometries. The P-1 model should typically be used for optical thicknesses (κL) > 1 [20], where κ is the absorption coefficient and L is the domain length scale. In the current simulation for the gaseous fuels, the scattering coefficient sets to zero, and it is assumed to be isotropic and the mean absorption coefficient of computational domain for all gases and all ranges of studied variables are $\cong$0.4 m^{-1} and hence κL is $\cong$1.04. Therefore, P-1 model is suitable to carry out the present work. The absorption coefficient value depends on the local concentrations of

H_2O and CO_2, path length and total pressure. To calculate κ, a weighted-sum-of-gray-gases model (WSGGM) is used as shown in Eq. (16),

$$-\nabla q_r = \kappa G - 4\kappa\sigma T^4. \quad (16)$$

The term $-\nabla q_r$ can be directly used into the energy equation to determine the radiation heat sources.

In the present study the governing equations are discretized using second order upwind interpolation scheme in CFD package and the PRESTO and SIMPLE algorithms for pressure interpolation and pressure–velocity are applied respectively. The solution is considered to be converged when the normalized residual of all variables including energy and radiation equations became the standard value of less than 10^{-5}. The Realizable k-ε turbulence model with standard wall functions (SWF) is used in the present simulation, where y+ > 5 in most of the kiln and with average value of 17.4. Therefore, it is concluded that the near-wall mesh resolution is acceptable in our problem to use SWF model.

4 Results and discussion

4.1 Shortcomings of PDF approach

In order to obtain the shortcomings of turbulence-chemistry interaction model (PDF approach), comparisons among the current numerical results and the published experimental results of Sandea and DLR presented by Meier et al. [19] for free jet flame are presented in Fig. 4a–h as was revealed by Elattar [18]. The figures present radial distribution for mixture fraction and temperature at $x/d_o = 60$, and axial mass fraction distribution for species including CH_4, H_2, O_2, H_2O, CO, and CO_2 at $T_{air} = T_o = 300$ K, $d_o = 8$ mm, $d_p = 140$ mm, $u_o = 42.2$ m/s and $u_p = 0.3$ m/s. Figure 4a–h reveals that the values obtained in this simulation study have similar trends of the published experimental data, but with higher values. The discrepancies between the simulation and experimental data are due to the assumptions made in the turbulence model, combustion model, and radiation model. In addition to turbulence-chemistry interaction model shortcomings and also due to the inaccuracy in experimental measurements.

In spite of satisfactory agreement obtained with experimental results [19], the shortcomings of the PDF model are evident. Figure 3a shows how the model tends to be under prediction of axial mixture fraction (f_a) along the flame as depicted in and over prediction for both the axial and radial temperature distributions (T_a and T_r) as shown in Figs. 3b and 4b, respectively. Low computed f_a is due to shortcoming of the PDF model, applying PDF method by under predicting the mixing process along the flame, thus the model under predicts the flame length. Moreover, the PDF model under predicts CH_4 and H_2 mass fractions in axial direction along the flame as presented in Fig. 4c, d. Nevertheless, Fig. 4g, h present how the PDF model over predicts the mass fractions of CO and CO_2 in axial positions along the flame, respectively. Furthermore, the PDF model predicts fairly the mass fraction of O_2 and H_2O along the flame as illustrated in Fig. 4e, f, respectively. Under predicting and over predicting of axial species mass fractions may be attributed to the shortcoming of the PDF model to predict perfectly the mixing process of reacting gases along the flame.

Additional comparison study is presented in Fig. 5a, b which shows comparisons between the current simulation and the experimental results presented by Kim et al. [26] for confined jet flame with and without radiation modelling which was presented by Elattar et al. [17]. Figure 5a displays axial temperature against axial mean mixture fraction with and without radiation modeling at $T_{air} = T_o = 300$ K, $d_o = 2.7$ mm, and $\lambda = 6.17$. As seen in the figure, the simulation data gives good agreement with experimental results. The discrepancies are due to turbulence, radiation and combustion models assumptions and simplifications and due to the experimental uncertainty. Additional comparison was conducted on the flame length for various fuel velocities (20–30 m/s) at $d_o = 2.7$ mm and 4.4 mm as presented in Fig. 5b. As shown in the figure, in case of radiation modeling consideration the simulated data gives perfect agreement with experimental data at small fuel nozzle diameter ($d_o = 2.7$ mm) and reveals satisfactory agreement for $d_o = 4.4$ mm. The discrepancies is due to the difference in definition the flame length between experimental and numerical determinations, all numerical assumptions and approximations and due experimental measurements uncertainty.

Despite of overall satisfactory agreement was obtained between the present simulation results with the experimental data of Kim et al. [26], the shortcomings of PDF approach are obvious. The model tends to under predict axial temperature and axial mean mixture fraction along the flame with radiation modeling and it reveals perfect fit without radiation modeling consideration. With radiation modeling, the PDF model under predicts the temperature and mean mixture fraction around the flame end (i.e. around f_{st}), otherwise it gives perfect predictions (near the burner tip and downstream the flame end). The possible explanation is that the PDF approach under predicts the mixing process at the flame end (at peak flame temperature) which leads to bad fuel and oxidizer mixing and hence lower temperature and mean mixture fraction can be obtained.

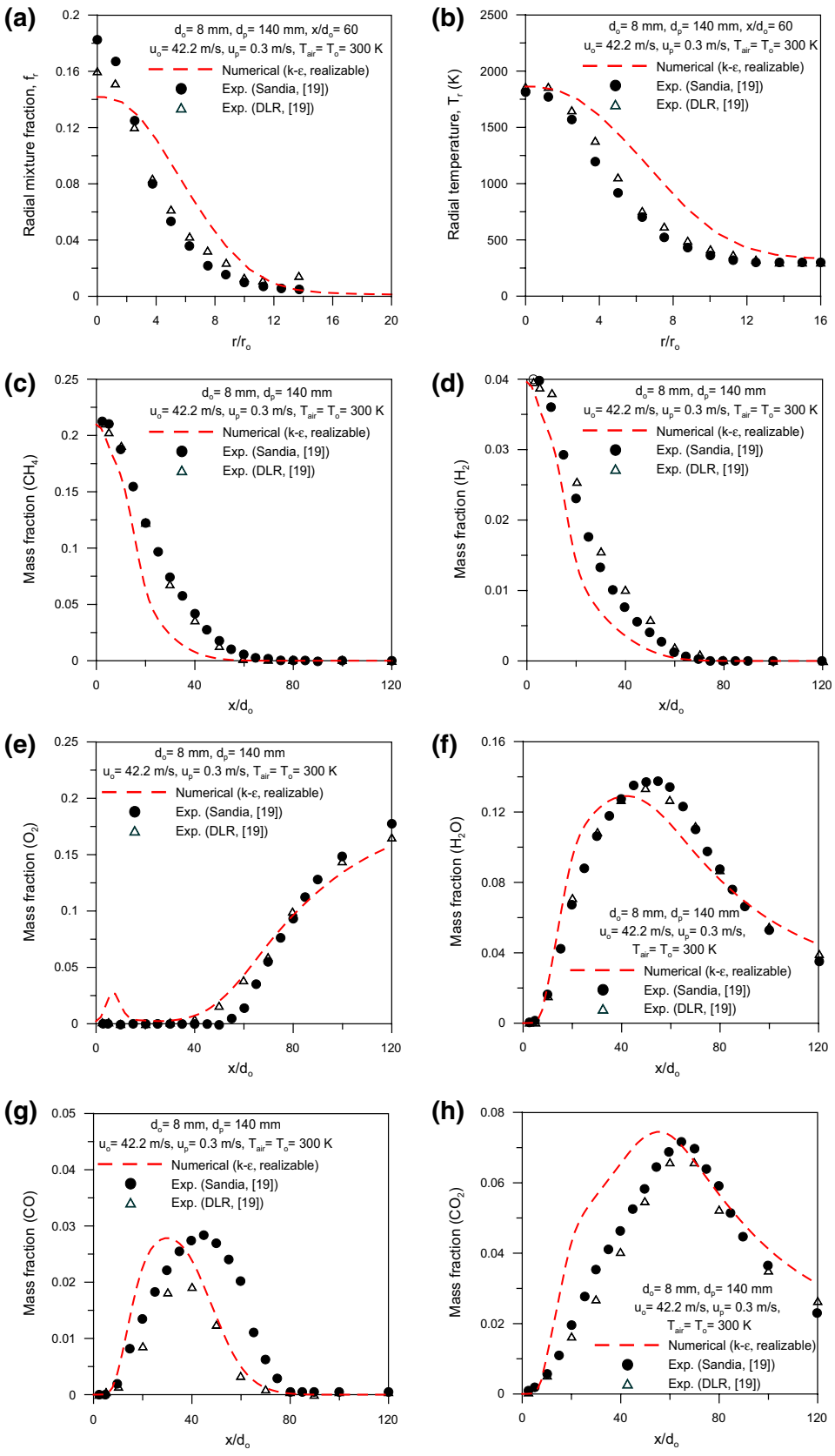

Fig. 4 Realizable k-ε turbulence model comparisons with experimental data [18]: **a** radial mean mixture fraction, **b** radial temperature, **c** axial centerline CH_4 mass fraction, **d** axial centerline H_2 mass fraction, **e** axial centerline O_2 mass fraction, **f** axial centerline H_2O mass fraction, **g** axial centerline CO mass fraction, **h** axial centerline CO_2 mass fraction

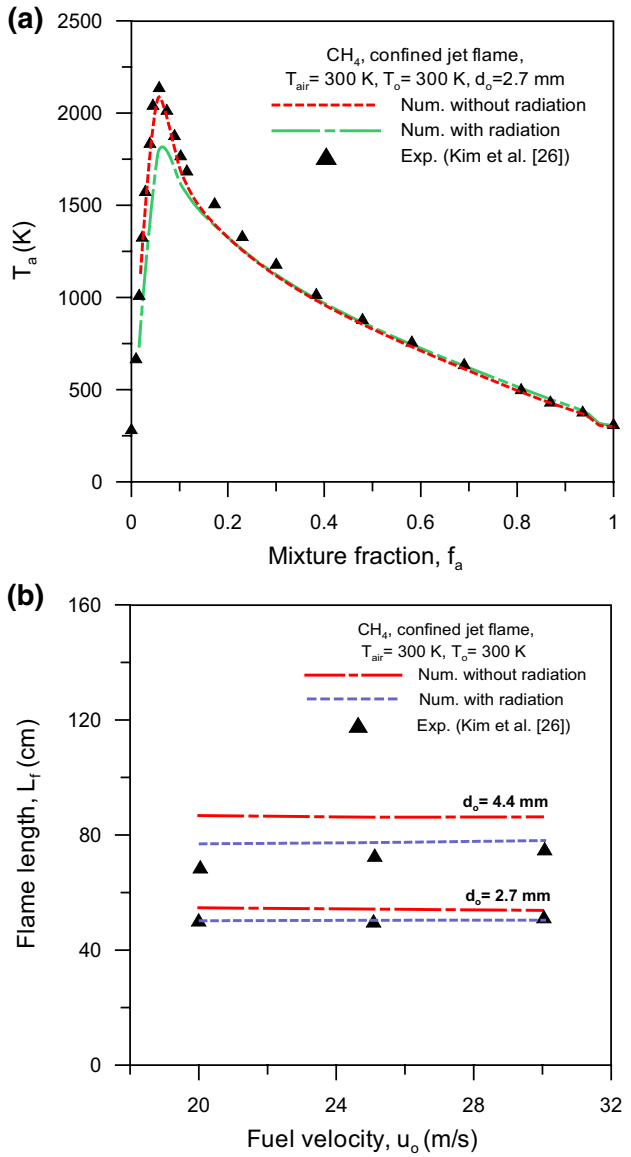

Fig. 5 Comparisons of simulated confined jet flame with experimental data with and without radiation modeling [17]: **a** axial centreline temperature versus mixture fraction, **b** flame length versus fuel velocity at different fuel nozzle diameters

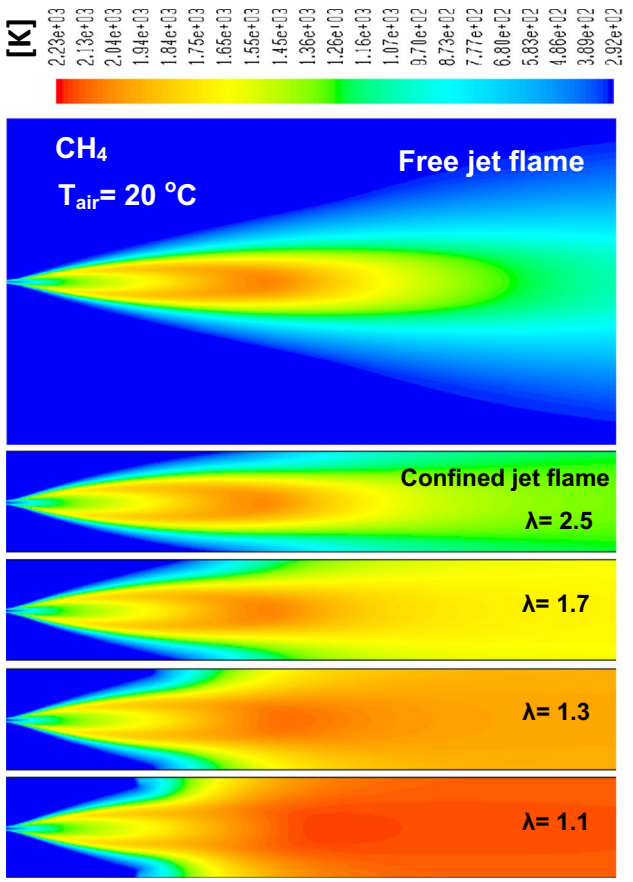

Fig. 6 Influence of excess air number on temperature contours using CH_4 fuel at $T_o = 20$ °C, $u_o = 30$ m/s and $d_{a,i}/D = 1$

4.2 Influence of excess air number (λ)

In the present study, the flame length is defined as the distance from the burner tip to the center of the flame where the mean value of the mixture fraction is equivalent to the stoichiometric value, f_{st} [27, 28]. Figure 6 shows the influence of excess air number (λ) that changes from 1 to 2.5 on temperature contours of rotary kiln flame in comparison with free jet flame using CH_4 fuel. As presented in Fig. 6, the high temperature zone area and the kiln flame volume decrease with increasing λ until the kiln flame becomes similar shape and length to free jet flame at λ = 2.5. This can be attributed to the small λ leads to slight amount of oxidizer (air) and thus the combustion could not be accomplished in short length and hence the flame must be diffused to complete its reaction. Figure 7a–c illustrate the influence of λ on the inverted dimensionless axial centerline mixture fraction profiles (f_o/f_a) for CH_4, *Biogas* and CO, respectively. As seen in Fig. 7, the flame length shortens with increasing λ and it becomes similar to free jet flame length at λ = 2.5. The possible explanation is due to the increase of λ means large quantity of air, thus, the combustion process can be fulfilled in small space and hence in short length. The same outcomes have been presented by Yang and Blasiak [29]. This means that the flame length attains to the shortest value in the case of highest λ, and this trend is similar for any tested fuels. For instance, the flame length of CH_4 fuel shortens by ≅7 % with increasing λ from 1.3 to 2.5.

4.3 Influence of kiln air entrance diameter ($d_{a,i}/D$)

Figure 8 shows the velocity vectors which are colored by temperature to present the influence of air entrance

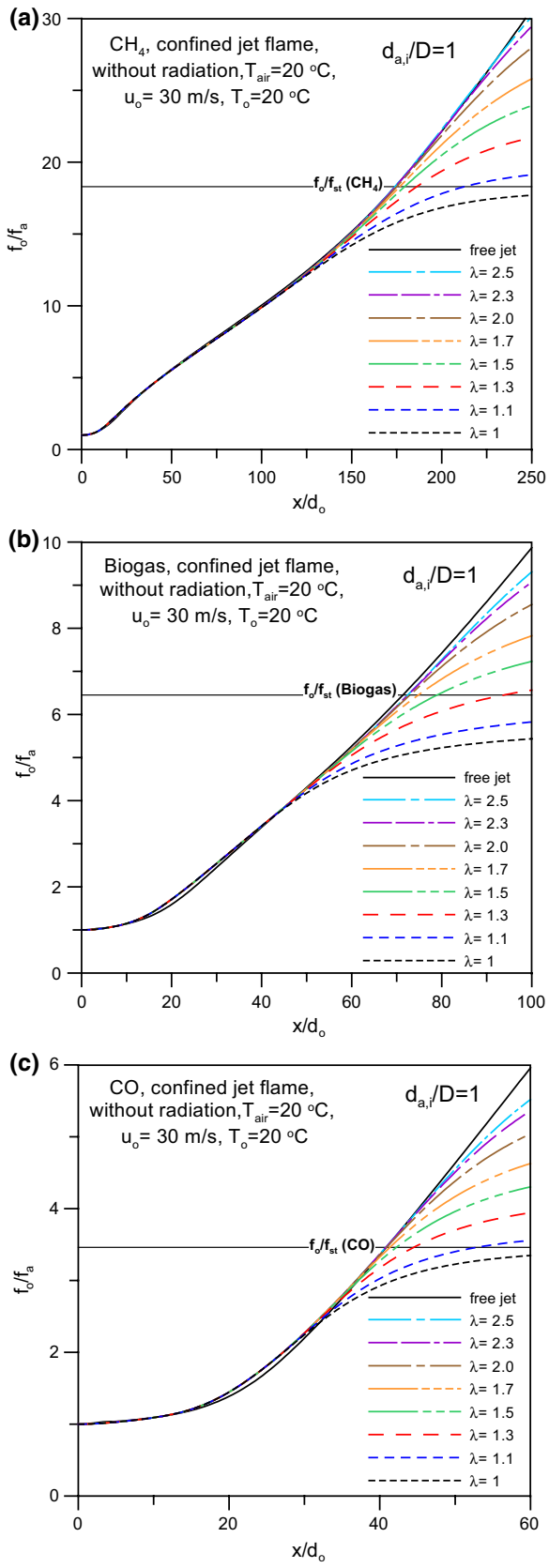

Fig. 7 Influence of excess air number on inverted dimensionless axial centerline mean mixture fraction for different fuels: **a** CH_4, **b** Biogas, **c** CO

diameter ($d_{a,i}/D$) that ranges from 0.06 to 1 on the flame aerodynamics (outer recirculation zones) for CH_4 flame at $\lambda = 1.3$. As illustrated in the figure, the recirculation zone length becomes less with increasing $d_{a,i}/D$, this is due to decreasing of axial air velocity (air momentum) with higher $d_{a,i}/D$ for the same λ which reduces the outer recirculation length and its strength. Moreover, decreasing $d_{a,i}/D$ increases the kiln entrance closed area that aids the recirculation eddies to occur and develop behind it. The influence of air entrance diameter on f_o/f_a profiles is shown in Fig. 9a–c to determine the flame lengths at $\lambda = 1.3$, 1.7, and 2.3, respectively. As displayed in the figure, the length of the flame shortens with decreasing $d_{a,i}/D$ and vice versa due to the increase in axial air velocity and outer recirculation eddies length due to the decrease in $d_{a,i}/D$ that leads to improve the mixing process between the fuel and the oxidizer, and hence the flame length shortens. In addition, varying $d_{a,i}/D$ (0.06–0.4) has a significant influence on the flame length, otherwise it has slightly effect. For instance, increasing $d_{a,i}/D$ from 0.06 to 0.4 causes an increase in the flame length by ~180 and ~6 % with increasing $d_{a,i}/D$ from 0.4 to 1 at $\lambda = 1.3$.

4.4 Influence of radiation modeling

Figure 10 shows the effect of radiation modeling on f_o/f_a profiles using CH_4 fuel for $d_{a,i}/D = 1$ with different λ (1.3, 1.7, and 2.3). As presented in the figure, the flame length is reduced by ~15, ~13, and ~12 % for $\lambda = 1.3$, 1.7, and 2.3, respectively under the radiation modeling condition. These reduction percentages in rotary kiln flame length are higher than that in free jet flame by ~4 % [30]. Figure 11 shows the reduction in flame length due to radiation modeling consideration presented by mean mixture fraction contours using CH_4 fuel at $\lambda = 1.3$. Shortening the flame length in case of radiation modeling consideration is due to part of heat released by radiation is added to the total heat released from the flame, hence, the peak flame temperature drops and shifts towards the burner tip. Whereas, the flame end is located around the peak flame temperature as proven and presented by Elattar [30].

4.5 Influence of fuel kinds

Figure 12 illustrates the effect of fuel kinds using CH_4, Biogas and CO gases on the flame length in rotary kilns presented by temperature contours without radiation modeling at $u_o = 30$ m/s, $\lambda = 2.3$, $d_{a,i}/D = 1$. As shown in the figure, CO fuel has the maximum peak flame temperature (~1950 °C) and the shortest flame length ($L_f/d_o \cong 41$). On the other side, Biogas fuel has the minimum peak flame temperature (~1550 °C) and has an intermediate flame length ($L_f/d_o \cong 73$). Whereas, the CH_4 fuel has

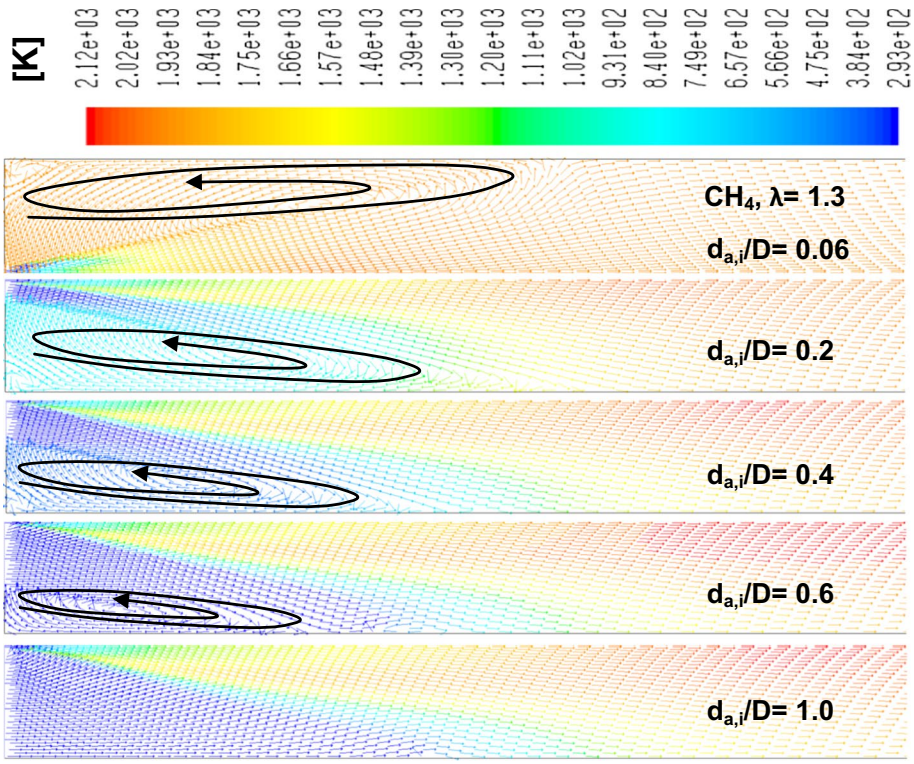

Fig. 8 Influence of dimensionless air entrance diameter on outer recirculation zones presented by velocity vectors *colored* by temperature using CH_4 fuel at $T_{air} = 20$ °C, $T_o = 20$ °C, $u_o = 30$ m/s and $\lambda = 1.3$

an intermediate peak flame temperature (~1800 °C) and has the longest flame length ($L_f/d_o \cong 174$). The possible explanation is that, the higher fuel stoichiometric air demand, the lower fuel stoichiometric mean mixture fraction can be obtained, hence, longer flame length can be revealed and vice versa. These outcomes are the same trends with the results of free jet flame simulation that presented by Elattar [30].

5 Flame length correlations

Figure 13a, b show predicted dimensionless correlations of rotary kiln flame length in terms of kiln geometric and operating parameters that was correlated by Elattar et al. [17]. The numerical correlation of dimensionless kiln flame length as a function in excess air number, stoichiometric air demand (mass basis), kiln air entrance diameter and diameter of the kiln is illustrated in Fig. 13a and has the following form:

$$\frac{L_f}{d_o} = 19.7\lambda^{-0.23}(1+L)^{0.8}\left(\frac{d_{a,i}}{D}\right)^{0.06}. \quad (17)$$

Equation (17) is in good standing with the following ranges:

$1.3 \le \lambda \le 2.5$, $2.46 \le L \le 17.3$, and $0.4 \le d_{a,i}/D \le 1$ at $T_{air} = T_o = 20$ °C. This correlation can calculate the majority of the results (83 %) within error of ±11 %. Moreover, the correlation demonstrates that the flame length is direct proportional with stoichiometric air demand and kiln air entrance diameter and reverse proportional with excess air number. Additional correlation for flame length as a function in excess air number, kiln air entrance diameter, stoichiometric mean mixture fraction, stoichiometric density and fuel density is correlated and illustrated in Fig. 13b. This correlation is developed in the same way as Eq. 17 and has the following form:

$$\frac{L_f}{d_o} = \frac{5.5}{f_{st}}\left(\frac{\rho_o}{\rho_{st}}\right)^{0.5}\left(\frac{1}{\lambda^{0.23}}\right)\left(\frac{d_{a,i}}{D}\right)^{0.06}. \quad (18)$$

Equation (18) is in good standing with the following ranges:

$1.3 \le \lambda \le 0.4$, $0.055 \le f_{st} \le 0.289$, and $0.4 \le d_{a,i}/D \le 1$ at $T_{air} = T_o = 20$ °C. This correlation can expect vast majority (98 %) of the numerical results at acceptable percentage error of ±11 %. Furthermore, the correlation shows that the flame length is direct proportional with fuel density and kiln air entrance diameter and reverse proportional with excess air number, stoichiometric density and stoichiometric mean mixture fraction.

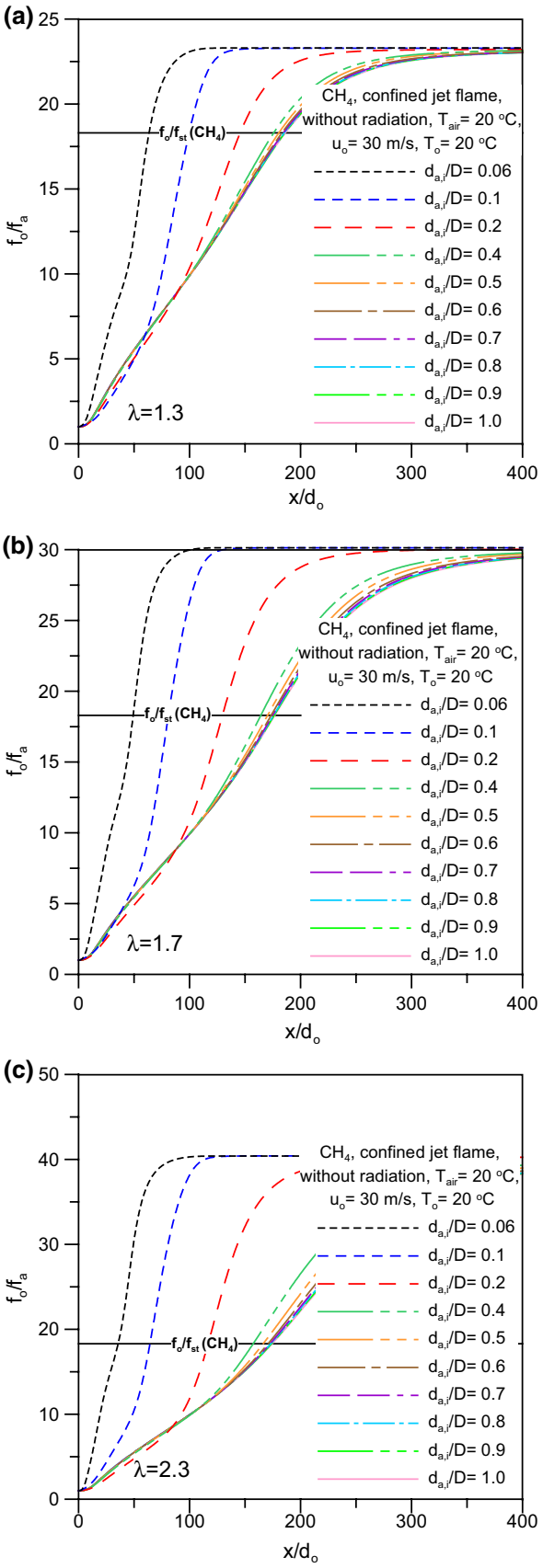

Fig. 9 Influence of dimensionless air entrance diameter on inverted dimensionless *axial centerline* mean mixture fraction using CH_4 fuel: **a** λ = 1.3, **b** λ = 1.7, **c** λ = 2.3

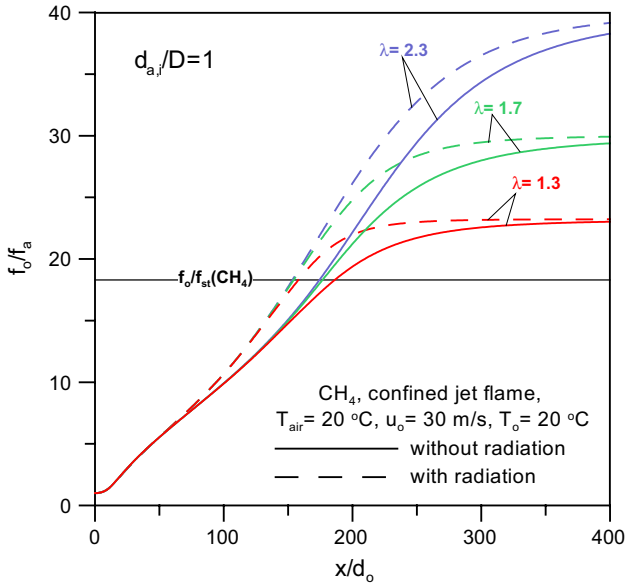

Fig. 10 Influence of radiation modeling on inverted dimensionless *axial centerline* mean mixture fraction profiles along the flame using CH_4 fuel at different excess air numbers

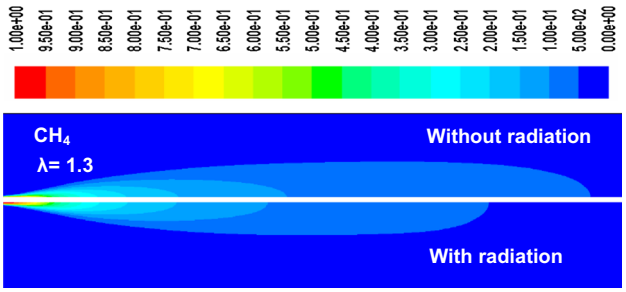

Fig. 11 Influence of radiation modeling on mean mixture fraction contours using CH_4 fuel at T_{air} = 20 °C, T_o = 20 °C, u_o = 30 m/s and λ = 1.3

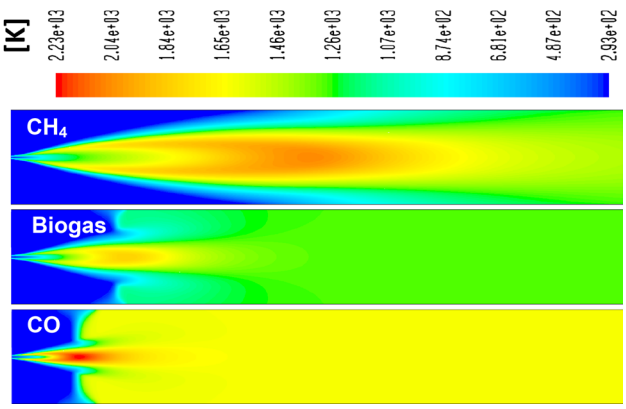

Fig. 12 Comparison of the flame lengths for different fuels presented by temperature contours at λ = 2.3, T_{air} = 20 °C, $d_{a,i}/D$ = 1 and u_o = 30 m/s

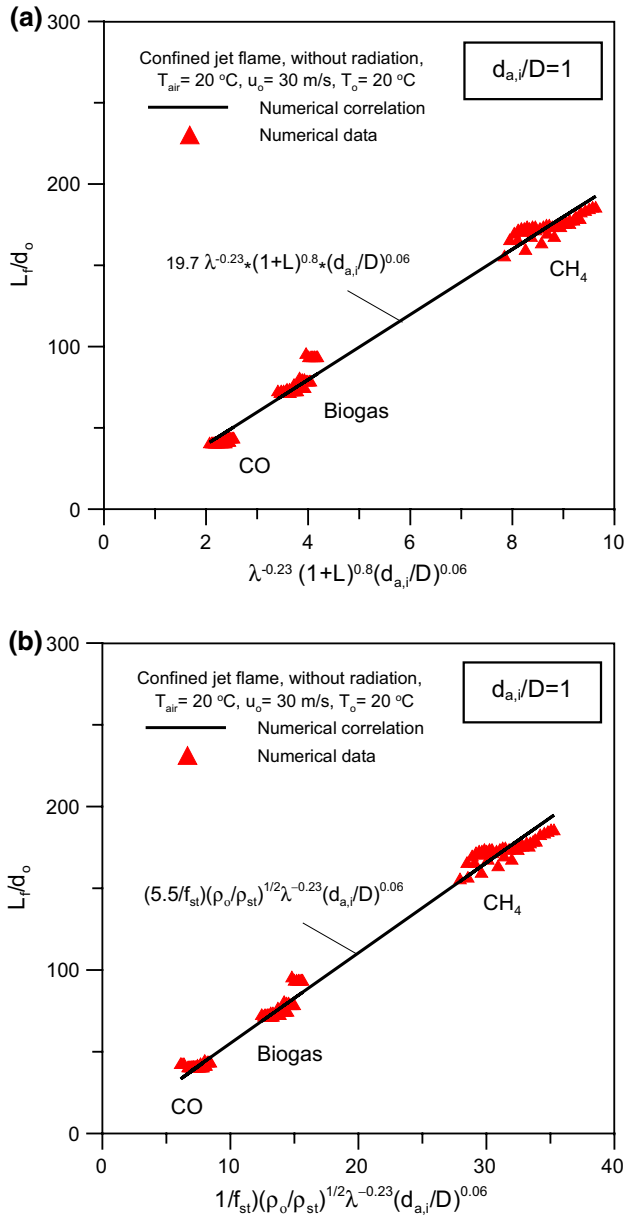

Fig. 13 Prediction of dimensionless rotary kiln flame length correlations [17] in terms of: **a** L, λ, $d_{a,i}/D$, **b** f_{st}, ρ_o, ρ_{st}, λ, and $d_{a,i}/D$

6 Conclusion

CFD modeling using PDF approach with realizable k-ε turbulence model is applied in the current study to present the effects of geometric and operating parameters of the rotary kiln on its flame lengths as sources of heat inside the kiln. Realizable k-ε turbulent model is chosen as the most effective turbulent model in comparison with the published experimental results. The findings show that the flame length is significantly influenced by excess air number, kiln air entrance diameter, radiation modeling consideration, and fuel type.

PDF approach reveals shortcomings despite of it gives overall satisfactory agreement with experimental data. It tends to under predict the mixture fraction, mass fractions of CH_4 and H_2 and over predict the temperature and the axial mass fractions of CO and CO_2 along the flame. Additionally, the PDF model under predicts the flame length.

Two numerical correlations for calculating the flame length of rotary kiln in dimensionless form are presented in terms of geometric and operating parameters of rotary kilns. The correlations are used to calculate the simulation results within adequate level of errors and also show that the flame length is direct proportional to stoichiometric air demand, fuel density and kiln air entrance diameter and reverse proportional to the excess air number, stoichiometric density and stoichiometric mean mixture fraction. Furthermore, the radiation modeling consideration has a significant influence on the shortening of the kiln flame length.

References

1. Boateng AA (2008) Rotary kilns transport phenomena and transport processes. ElsevierInc, Oxford
2. Jauhari R, Gray MR, Masliyah JH (1998) Gas–Solid mass transfer in a rotating drum. Can J Chem Eng 76(2):224–232
3. Georgallis M (2004) Mathematical modeling of lime kilns. Ph.D. Dissertation, The University of British Columbia, Vancouver, BC
4. Peray KE (1972) The rotary cement kiln. Chemical Publishing Co., New York
5. Manitius A, Kureyuz E, Kawecki W (1974) Mathematical model of the aluminium oxide rotary kiln. Ind Eng Chem Process Des Dev 13(2):132–142
6. Bui RT, Simard G, Charette A, Kocaefe Y, Perron J (1995) Mathematical modeling of the rotary coke calcining kiln. Can J Chem Eng 73(4):534–545
7. Smidth F, "Duoflex® Burner," flsmidth (2015) http://www.flsmidth.com/en-US/Industries/Cement/Products/Pyroprocessing/Duoflex+Burner/Duoflex+Burner. Accessed 10 April 2015
8. Rovaglio M, Manca D, Biardi G (1998) Dynamic modeling of waste incineration plants with rotary kilns: comparisons between experimental and simulation data. Chem Eng Sci 53(15):2727–2742
9. Abe I, Fukuhara T, Iwasaki S, Yasuda K, Nakagawa K, Iwata Y, Kominami H, Kera Y (2001) Development of a high density carbonaceous adsorbent from compressed wood. Carbon 39(10):1485–1490
10. Miguel GS, Fowler GD, Dall'Orso M, Sollars CJ (2002) Porosity and surface characteristics of activated carbons produced from waste tyre rubber. J Chem Technol Biotechnol 77(1):1–8
11. Ortiz OA, Sua'rez GI, Nelson A (2005) Dynamic simulation of a pilot rotary kiln for charcoal activation. Comput Chem Eng 29(8):1837–1848
12. Cook CA, Cundy VA (1995) Study of parameters influencing wall-to-bed heat transfer in low-temperature rotary desorbers. J Energy Resour Technol, Trans ASME 117(1):50–57
13. Rensch T (2001) Beitrag zum Prozess der thermischen Bodendekontamination im Drehrohrofen. Ph.D. Dissertation, The University of Magdeburg, Germany
14. Barr P (1986) Heat transfer processes in rotary kilns. Ph.D. Dissertation, The University of British Columbia, Vancouver, BC

15. Kolev D, Stefanov B, Borisov D, Choshnova D (2003) Method for numerical simulation and graphical presentation of the rate field in a physical model of flash smelting furnaces. J UCTM 38(4):1147–1154
16. Aloqaily A (2008) A study of aerodynamics in rotary kilns with two burners. Ph.D. Dissertation, The University of Toronto, Canada
17. Elattar HF, Stanev R, Specht E, Fouda A (2014) CFD simulation of confined non-premixed jet flames in rotary kilns for gaseous fuels. Comput Fluids 102(10):62–73
18. Elattar HF, Specht E, Fouda A, Bin-Mahfouz AS (2016) Study of parameters influencing fluid flow and wall hot spots in rotary kilns using CFD. Can J Chem Eng 94(2):355–367
19. Meier W, Barlow RS, Chen Y, Chen J (2000) Raman/rayleigh/lif measurements in a turbulent ch4/h2/n2 jet diffusion flame: experimental techniques and turbulence-chemistry interaction. Combust Flame 123(3):326–343
20. ANSYS, Inc. (2011) ANSYS FLUENT User's guide. Ansys Inc, Canonsburg
21. Moles FD, Watson D, Lain PB (1973) The aerodynamics of the rotary cement kiln. J Inst Fuel 46:353–362
22. Shih TH, Liou WW, Shabbir A, Yang Z, Zhu J (1995) A new k-ε eddy viscosity model for high reynolds number turbulent flows. Comput Fluids 24(3):227–238
23. Poinsot T, Veynante D (2001) Theoretical and numerical combustion. R.T. Edwards, Inc, Philadelphia
24. Cheng P (1964) Two-dimensional radiating gas flow by a moment method. AIAA J 2:1662–1664
25. Siegel R, Howell JR (1992) Thermal radiation heat transfer. Hemisphere Publishing Corporation, Washington DC
26. Kim HK, Kim Y, Lee SM, Ahn KY (2007) Studies on combustion characteristics and flame length of turbulent oxy-fuel flames. Energy Fuels 21(3):1459–1467
27. Hawthorne WR, Weddell DS, Hottel HC (1949) Mixing and combustion in turbulent gas jets. Symp Combust Flame, Explos Phenom 1(3):266–288
28. Peters N (2000) Turbulent combustion. Cambridge University, Cambridge
29. Yang W, Blasiak W (2004) Chemical flame length and volume in liquified propane gas combustion using high-temperature and low-oxygen-concentration oxidizer. Energy Fuels 18(5):1329–1335
30. Elattar HF (2011) Flame simulation in rotary kilns using computational fluid dynamics, Ph.D. Dissertation, Magdeburg University, Germany